Seismic Tremor Reveals Spatial Organization and Temporal Changes of Subglacial Water System

A Thesis
Presented in Partial Fulfillment of the Requirements for the
Degree of Master of Science
with a
Major in Geography
in the
College of Graduate Studies
University of Idaho
by
Margot E. Vore

Major Professor: Timothy C. Bartholomaus, Ph.D.
Committee Members: Paul Winberry, Ph.D., Kenneth Sprenke, Ph.D. Vladimir Aizen, Ph.D.
Department Administrator: Leslie Baker, Ph.D.

May 2018

Authorization to Submit Thesis

This thesis of Margot E. Vore, submitted for the degree of Master of Science with a Major in Geography and titled "Seismic Tremor Reveals Spatial Organization and Temporal Changes of Subglacial Water System," has been reviewed in final form. Permission, as indicated by the signatures and dates below, is now granted to submit final copies to the College of Graduate Studies for approval.

Major Professor: _____ Date:_____
Timothy C. Bartholomaus, Ph.D.

Committee Members: _____ Date:_____
Paul Winberry, Ph.D.

_____ Date:_____
Kenneth Sprenke, Ph.D.

_____ Date:_____
Vladimir Aizen, Ph.D.

Department Administrator: _____ Date:_____
Leslie Baker, Ph.D.

Abstract

Subglacial water flow directly impacts glacier dynamics and shapes the subglacial environment. The subglacial water system changes in response to water that flows through conduits at the glacier's bed, with a distributed, inefficient drainage system in the winter evolving into a channelized, efficient system during the melt season. Due to the challenges of observing glacier beds, the spatial organization of subglacial water systems and the time scales of conduit evolution and migration are unknown. To address these questions, I monitor seismic tremor produced by subglacial water flow, i.e. glaciohydraulic tremor, between 1.5 and 10 Hz throughout the 2016 melt season on Taku glacier. I use frequency dependent polarization analysis to estimate glaciohydraulic tremor propagation direction (which is a proxy for subglacial conduit location) and a degree day melt model to monitor trends of melt water input. This study reveals that conduit formation relies on sustained water input and that single conduit flow paths can be distinguished from multi-conduit flow paths. Seismic tremor from multi-conduit flow experiences multiday locational changes while tremor produced by single conduit flow remains more stationary. This study also provides insight into the frequency, propagation, and wave structure of glaciohydraulic tremor, with polarized glaciohydraulic tremor wave types potentially linked to the distance from source to station and multiple frequencies propagating from the same source direction with propagation constrained by a distance threshold. My findings clarify the development and spatial organization of subglacial water systems which may be applied in future studies to gain a better understanding of glacier sliding speeds and glacier dynamics.

Acknowledgments

I want to thank all the people who have contributed to this project: Dr. Jason Amundson at University of Southeast Alaska, Dr. Paul Winberry at Central Washington University for contributing data set to the project, and Dr. Jake Walter from the University of Texas: Institute of Geophysics for developing this project idea in tandem with Dr. Timothy C. Bartholomaus at the University of Idaho. I would also like to thank Taylor Borgfeldt from University of Texas: Institute of Geophysics who helped with the retrieval of seismometers from Taku glacier.

Thanks to my committee members Dr. Kenneth Sprenke, Dr. Paul Winberry, and Dr. Valdimir Aizen.

I also want to give a special thanks to Dr. Timothy C. Bartholomaus who took a chance bringing me on as his first ever graduate student. Thanks to his patience, knowledge, kindness, and enthusiasm, I have found a subject I am passionate about and grew into a well-rounded academic.

Dedication

I would like to dedicate this work to my parents, Jean and Nelson Vore, who have always been there when I need support, encouraging words, a gentle push, or love. Without them behind me, I could not have succeeded in school or had the courage to venture off on my own. I cannot put into words how much appreciation I have for them and how grateful I am to call them my parents.

Table of Contents

List of Figures

1. Introduction

Hundreds of meters of glacier ice prevent direct observation of glacier beds and limit our understanding of subglacial landscapes and their morphology. Subglacial landscapes are sculpted by the interaction between subglacial water flow and the overburden pressure exerted by glaciers on their beds. This interaction between overburden pressure and water flow creates an annual cycle that transforms the subglacial water system from an inefficient distributed system in the winter to an efficient channelized system during the melt season [*Fountain and Walder*, 1998; *Cowton et al.*, 2013; *Chu*, 2014]. While this annual cycle has been broadly described, the spatio-temporal evolution of subglacial conduits remain poorly known, including their number, location, and potential migration. Due to the influence subglacial water flow has on glacier sliding speeds [*Iken and Bindschadler*, 1986; *Bartholomaus et al.*, 2008; *Bartholomew et al.*, 2010; *Gimbert et al.*, 2016], locating and tracking temporal changes of these subglacial conduits is likely to lead to better constraints on glacier dynamics.

Seismology has the potential to continuously monitor the evolution of the subglacial water system. Terrestrial rivers and streams produce high frequency (>1 Hz) ambient seismic noise tremor, through turbulent water flow and sediment transport [*Burtin et al.*, 2008; *Tsai et al.*, 2012; *Schmandt et al.*, 2013, 2017; *Gimbert et al.*, 2014]. . Flowing water in subglacial conduits also produces ambient seismic noise, known as glaciohydraulic tremor, which is a proxy for subglacial water flow [*Bartholomaus et al.*, 2015]. Bartholomaus et al. [2015] explored the correlation between ambient seismic noise and its potential sources such as basal sliding, calving, subglacial water flow, and rain events. They conclude that the tremor signal between 1.5 and 10 Hz on Yahtse glacier and Mendenhall glacier is due to subglacial water flow, indicating that seismology can inform our understanding of subglacial conduits, potentially including their locations and temporal evolution.

There are a limited number of methods capable of locating tremor sources. Beamforming [*Rost and Thomas*, 2002], which was successfully used to track temporal changes in tremor during a transient subglacial flood [*Winberry et al.*, 2009], is the only method that has been utilized to locate glaciohydraulic tremor thus far. However, there are many methods that are used to track earthquakes and volcanic tremor which may be applicable in a glacial setting. Cross correlation, which requires coherent seismic signals with significant structure, has been used to locate tremor sources within the earth's crust and around

subduction zones [*Obara*, 2002; *Wech and Creager*, 2008] while backprojection was utilized by Haney [2014] to track changes in volcanic tremor. Frequency dependent polarization analysis (FDPA), which was first introduced in Park et al. [1987], has also been used in various studies [*Koper and Hawley*, 2010; *Koper and Burlacu*, 2015; *Workman et al.*, 2016; *Goodling et al.*, 2018] to track locations of microseisms, ambient seismic noise, and hydraulic sources in settings throughout the United States. FDPA relies on a single 3-component seismometer rather than a tight array of instruments, which beamforming, cross correlation, and backprojection all require.

In this study, I use frequency dependent polarization analysis (FDPA) to quantify the polarization of glaciohydraulic tremor waveforms, to determine the dominate wave type of tremor, to identify the frequencies containing glaciohydraulic tremor, and to determine the source location of tremor on Taku glacier, a temperate valley glacier located to the northeast of Juneau, Alaska , over the 2016 melt season. Glaciohydraulic tremor source locations that are calculated using FDPA are used as a proxy for the location of subglacial conduits or dominant subglacial water features. A degree day melt model in tandem with analysis of temporal changes in glaciohydraulic tremor locations and power correlations reveal the organization of the subglacial water system as well as time scales of conduit evolution and migration. This study also provides insight into the frequency, propagation, and wave structure of glaciohydraulic tremor signals as well as the relationship between water input and glaciohydraulic tremor power.

2. Research Site

To explore the connections between an evolving subglacial hydrologic network and seismic tremor, I draw on data acquired at Taku glacier, a temperate valley glacier located to the northeast of Juneau, Alaska. Taku glacier is one of the thickest temperate glaciers in the world, with a maximum ice thickness of about 1,477 m [*Nolan et al.*, 1995]. Taku has advanced over 7 km since the 1890's, which has resulted in the disappearance of Taku fjord [*Motyka et al.*, 2006; *Larsen et al.*, 2007]. This advance is attributed to the filling of Taku inlet

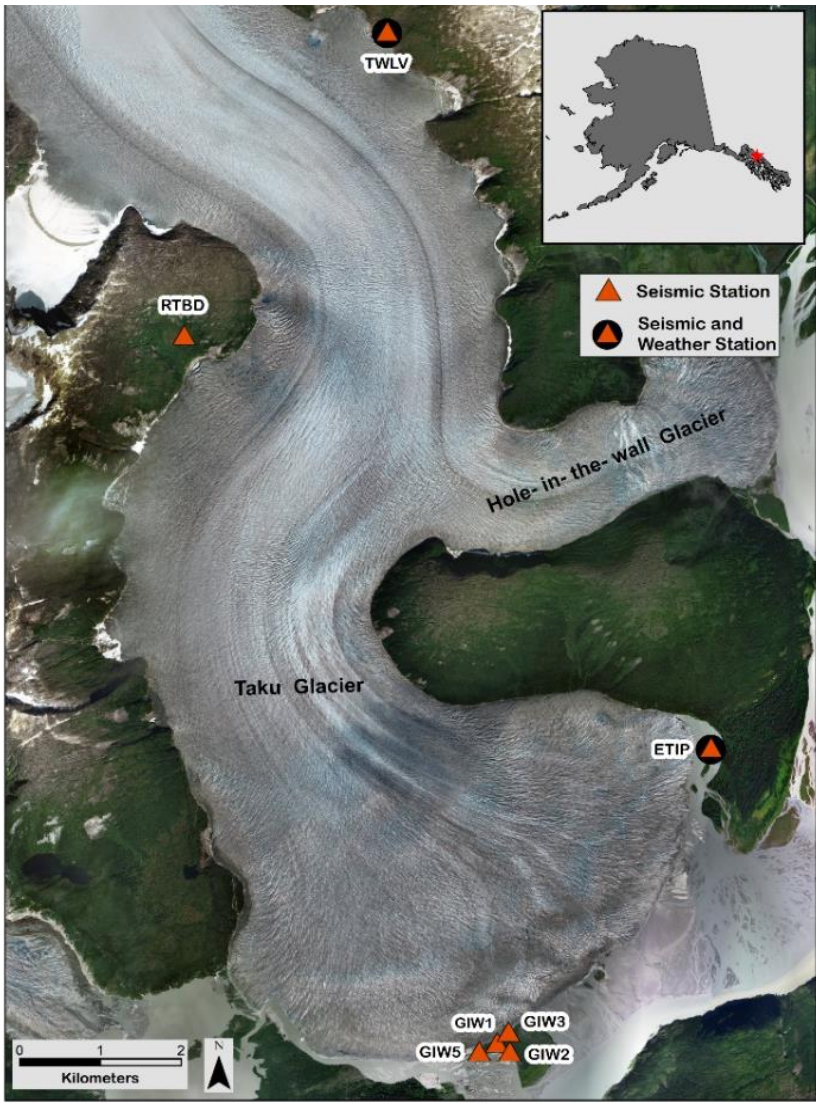

Figure 2.1: Map of seismic and weather stations in the ablation area of Taku glacier. Instrumentation was deployed from March- October 2016. The orange triangles represent locations of seismometers, with stations surrounded by black circles representing seismometers that are collocated with weather stations. Background: Composite of WorldView 2 and 3 satellite sensor imagery from 2013 and 2015 (Source: DigitalGlobe, Inc.)

with sediment which has slowed the speed of iceberg calving [*Post and Motyka*, 1995]. Large melt volumes occur each year on Taku glacier, with nearly 8.7 m of snow water equivalent melting from terminus point locations in 2016. Existing theory [*Fountain and Walder*, 1998; *Cowton et al.*, 2013] predicts that these high melt volumes should produce an efficient drainage system beneath Taku glacier, leading to strong glaciohydraulic tremor signals on and around the glacier [*Bartholomaus et al.*, 2015].

From March to October 2016, seven 3-component, broadband seismometers were placed in the ablation area of Taku glacier. Figure 2.1 shows a map of Taku glacier's terminus and the locations of instrumentation. All seismometers are Nanometric Meridian Compact Posthole sensors with a 120 s low-frequency corner, sampling at 200 Hz. ETIP, RTBD, and TWLV were buried off-ice approximately 15 cm below the surface and the remaining four seismometers were buried off-ice at a depth of about 1 m. In most cases, power failures and wildlife damage prevented the recording of continuous records. Taku River is less than 1 km away from to the GIW array, located at the southern terminus, as well as station ETIP at the southeast terminus. ETIP is located on a sand bar in the middle of a small outlet stream (< 250 m wide) that flows out of Taku glacier. This small stream separates ETIP from the glacier.

Weather stations, co-located with seismic stations ETIP and TWLV (Fig. 2.1), were also deployed during the collection period. Humidity, wind, and temperature data were collected at both weather stations using a Vaisala WXT520 sensor recording at 10 min time intervals. Rain data was collected at ETIP using an Onset HOBO tipping bucket rain gauge, with each tip representing 0.2 mm of precipitation.

3. Methods

3.1- Frequency dependent polarization analysis

The configuration of seismic stations at Taku glacier is designed to track the broad spatial evolution of tremor along the glacier length as well as the wave structure of glaciohydraulic tremor, which has no discernable onset or structure at timescales shorter than minutes. Thus frequency dependent polarization analysis (FDPA) [*Park et al*., 1987] rather than cross correlation, back projection, or beamforming is used as my primary analysis method to determine the wave type, polarization, and backazimuth of glaciohydraulic tremor signals. Additional clarification of this method is provided in Koper and Hawley [2010], Koper and Burlacu [2015], and Workman et al. [2016], who utilized the method to track ambient seismic noise throughout the United States. The work flow is presented in a flow chart in Figure 3.1.

This analysis begins with a three-component seismic signal spanning one day,

$$x(t) = [\, Z(t), N(t), E(t) \,], \qquad (1)$$

with Z representing the vertical channel and N and E representing the north and east channels respectively. *x(t)* is placed through a 0.5 Hz high pass filter to remove microseisms and is demeaned. $x(t)$ is then split into one-minute subsets with 50% overlap,

$$x_n(t) = [\, Z_n(t), N_n(t), E_n(t)] \text{ with } n \in \{1, \dots, 2879\}, \qquad (2)$$

where *n* represents the subset number. For each channel in subset *n*, a Fourier transform with a prolate spheroidal taper, to reduce spectral leakage, is used

$$x_n(t) \rightarrow X_n(f) = [\, Z_n(f), N_n(f), E_n(f)] \qquad (3)$$

which transforms the seismic signal into the frequency domain. Each row of $X_n(f)$ represents a different frequency within the signal.

Thirteen consecutive one-minute subsets are then grouped, with each matrix group representing the spectra of seven minutes of seismic signal over the day long record. Grouping the subsets allows for backazimuths to be calculated over small time windows, which can then be binned over longer time periods to produce probabilities of source locations.

For frequency *f*, an average spectral covariance matrix, M_a, is calculated for each seven-minute grouping. For the j^{th} matrix in a given seven-minute group, where $j \in \{1, \dots, 13\}$, a 3 x 3 spectral covariance matrix is calculated by multiplying the row of X_n associated with frequency *f* with its complex conjugate

$$M_j(f) = X_j(f)^H \cdot X_j(f) \tag{4}$$

The real and imaginary parts of the thirteen spectral covariance matrices are separately, linearly averaged and then recombined to create an average spectral covariance matrix, M_a

$$M_a(f) = \frac{\sum_{j=1}^{13} Re(M_j(f))}{13} + \frac{\sum_{j=1}^{13} Im(M_j(f))}{13} \tag{5}$$

which represents an average seven-minute seismic signal at frequency *f*. Averaging of the thirteen spectra in a group matrix prevents short term transient events or signal noise from interfering with backazimuth estimates.

A singular value decomposition of the average spectral covariance matrix,

$$M_a = UDV^H \tag{6}$$

produces left eigenvectors, $U = [\boldsymbol{U_1}, \boldsymbol{U_2}, \boldsymbol{U_3}]$, right eigenvectors, $V^H = [\boldsymbol{V_1}, \boldsymbol{V_2}, \boldsymbol{V_3}]$, and singular values

$$D = \begin{bmatrix} d_1 & 0 & 0 \\ 0 & d_2 & 0 \\ 0 & 0 & d_3 \end{bmatrix}$$

Each singular value, d_i, represents the average seismic energy, at a given frequency, within the plane of motion defined by its eigenvector. If $d_1 >> d_2$ and d_3, then

$$Z_p = V_1^T = [\, A_z e^{-i\varphi_z}, A_x e^{-i\varphi_x}, A_y e^{-i\varphi_y} \,] \tag{7}$$

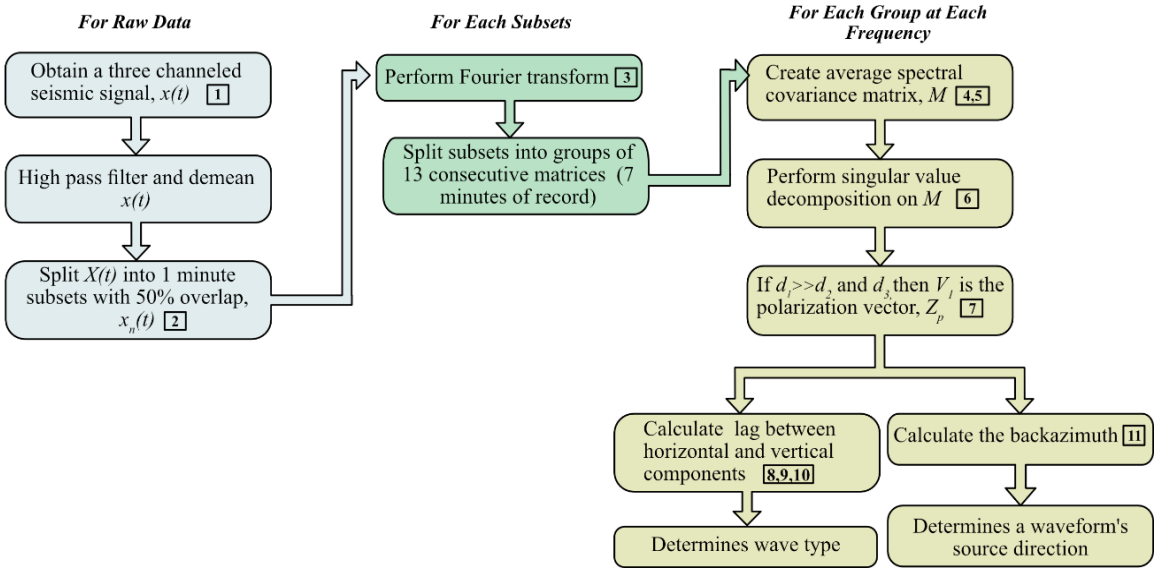

Figure 3.1: Flow chart of wave polarization analysis method. Boxed numbers identify the equation(s) related to a given step.

where Z_p is the polarization vector. Z_p consists of three complex values that contain both amplitude (A_i) and phase (φ_i) components with the real component vector and imaginary component vector spanning the waveform's dominant plane of motion.

To determine the wave type associated with the average seven-minute seismic signal, the phase lag between the horizontal and vertical components, φ_{VH}, is calculated. The phase of the horizontal components, φ_H, is equal to the ωt

$$\omega t = -\frac{1}{2}\arg\left(\left(A_x e^{-i\varphi_x}\right)^2 + \left(A_y e^{-i\varphi_y}\right)^2\right) + l\pi/2 \quad \text{where } l \text{ is an integer} \tag{8}$$

that maximizes

$$A_H = \left[\left(A_x \cos(\omega t + \varphi_x)\right)^2 + \left(A_y \cos\left(\omega t + \varphi_y\right)\right)^2\right] \tag{9}$$

with equations 8 and 9 determining the dominate direction of horizontal motion.

Once φ_H is determined, the lag between horizontal and vertical components is calculated

$$\varphi_{VH} = \varphi_H - \varphi_z \tag{10}$$

where φ_z is the phase of the vertical component. φ_{VH} is bounded between -90˚ and 90˚, with $\varphi_{VH} > |90|$ equivalent to $\varphi_{\mathrm{VH}} + \pi$. A phase lag between the horizontal and vertical component that is close to zero represents a body wave with planar particle motion and $|\varphi_{\mathrm{VH}}| = 90$ is indicative of a Rayleigh wave.

Once the polarization vector has been identified, the backazimuth, θ, of the waveform is calculated

$$\theta = \tan^{-1}\left(\frac{A_y}{A_x}\right) \tag{11}$$

FDPA can only determine backazimuths of Rayleigh waves due to their distinct elliptical (rather than planar) motion.

3.2- Constraints of glaciohydraulic tremor

Prior to identifying a backazimuth towards a glaciohydraulic tremor source, I apply three constraints to identify those frequencies and time periods containing locatable tremor. First, for glaciohydraulic tremor to be present, a peak in seismic power must occur as high powered tremor signals are known to be produced by subglacial water flow [*Bartholomaus et al.*, 2015]. Considering FDPA only calculates backazimuths of polarized, Rayleigh waves, I also require that glaciohydraulic tremor to be strongly polarized (i.e., particle motions well

constrained within a dominant plane of motion) and consist predominantly of Rayleigh waves. I consider the frequencies of a given day where these all three of these criteria are met as the frequencies and times containing glaciohydraulic tremor that can be located using FDPA. I further describe the implementation of these criteria in the following paragraphs.

The first constraint to identify glaciohydraulic tremor frequencies is that seismic power must be unusually strong, both in terms of time and in terms of frequency. Median power spectrograms, created by finding the median power spectral density of one hour of vertical component data (with the median representing 1 hour of data) [*Bartholomaus et. al*, 2015] allows for the identification of these patterns (Fig. 3.2). Glaciohydraulic tremor frequency bands contain power peaks that begin early in the melt season and progressively intensify throughout the summer months which is thought to be due to the gradual formation of subglacial conduits that move large volumes of water [*Bartholomaus et. al*, 2015]. Thus, high powered frequency bands that persist throughout the melt season are considered to represent glaciohydraulic tremor. These distinct high-powered bands predominantly occur between 1.5 and 10 Hz (Fig. 3.2), consistent with the findings of Bartholomaus et al. [2015].

Frequencies that exhibit peaks in seismic power are determined by analyzing a smoothed daily PSD of vertical ground motion. The power differences, D_1 and D_2, between a given power value, γ, and its two surrounding local minimum values, m_1 and m_2, are calculated and compared to a threshold value, h (Fig. 3.3). I choose the 50th percentile of all differences

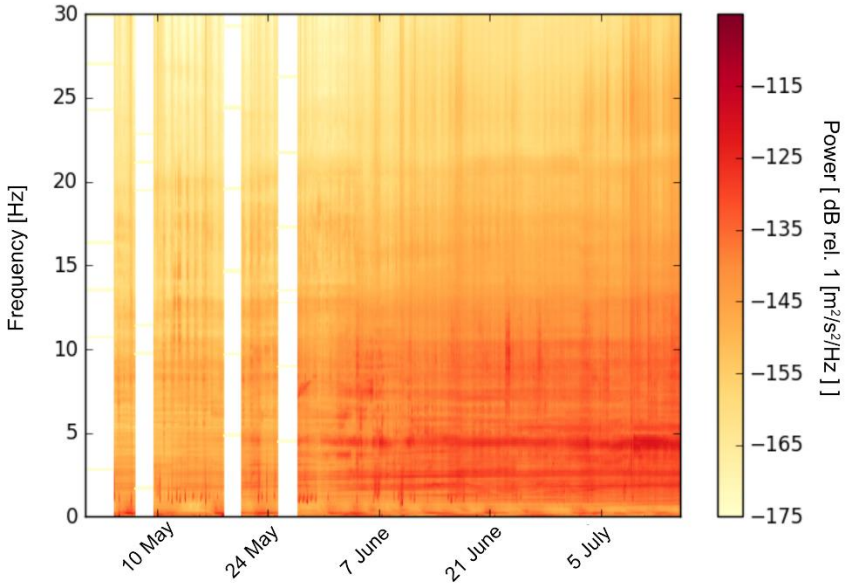

Figure 3.2: Median power spectrogram from the vertical component at station ETIP. Horizontal banding (representing strong seismic power with stable frequencies) occur in distinct frequency ranges between 1.5 and 10 Hz.

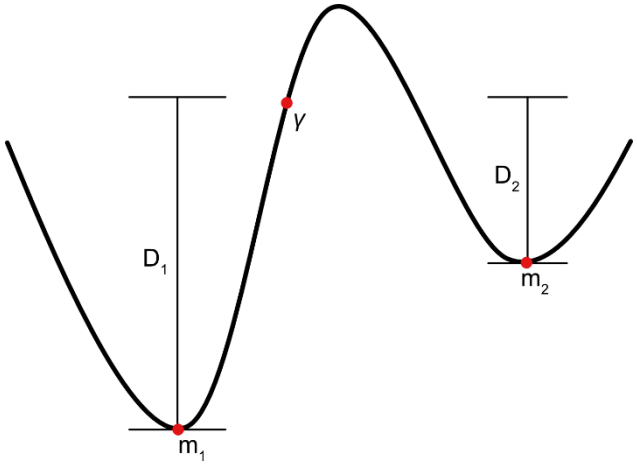

Figure 3.3: An example showing how peaks in median power spectral density are calculated. D_1 and D_2 are the vertical distances between a power γ and its two surrounding minimum values m_1 and m_2. If both D_1 and D_2 are greater than a threshold value, h, then γ is considered to represent a peak in seismic power.

between consecutive local minimum and maximum values for the last two weeks of data at a given station between 1.5 and 10 Hz to represent the threshold *h*. The last two weeks of data for a given station have the largest power peaks, as the most subglacial water flow is occurring, thus this time span best represents peaks in seismic power. This method allows a different threshold value for each seismic station to compensate for varying ranges of seismic power at each collection site. If D_1 and D_2 both exceed the threshold value *h* of a respective station, then I consider the power, γ, to represent a peak in seismic power. An example of power peak selection can be seen in figure 3.4A.

For FDPA to calculate backazimuths of glaciohydraulic tremor, frequencies that contain tremor must also be strongly polarized. Waveforms with strong polarization contain a large portion of its seismic energy in a single plane of motion indicating an organized seismic signal and coherent arrivals (presumably from a single direction). The extent of wave polarization is determined by the ratio between the first and second singular values of the waveform (eq. 6), where frequencies with a ratio greater than 2.5 are considered to be strongly polarized (Fig. 3.4b). The threshold value of 2.5 was selected as it encompasses qualitatively identified polarization peaks while excluding troughs in polarization values at all stations except ETIP (which has unusually large polarization values). A polarization threshold value of 3 begins to exclude qualitatively identified peaks in ratio values while a polarization threshold of 2 is too inclusive of troughs in the polarization values.

Finally, for FDPA to calculate backazimuths, glaciohydraulic tremor frequencies must have a consistent phase lag between the waveform's horizontal and vertical planes of motions that are indicative of Rayleigh waves. Peaks in wave type are identified by comparing the daily percentage of wave forms of a given phase lag to a threshold value, with phase lags categorized into three groups: Rayleigh waves, body waves, and mixed waves. For classification purposes, I define Rayleigh waves as having an absolute phase lag between 70˚ and 90˚ (signifying defined elliptical particle motion), body waves having 0˚ to 20˚ absolute phase lag (signifying rectilinear motion), and mixed waves with a 20˚ to 70˚ absolute phase lag. Mixed waves are those that do not fall into the other two categories. While Love waves also exhibit rectilinear motion, I require all waves to have power peaks in the vertical

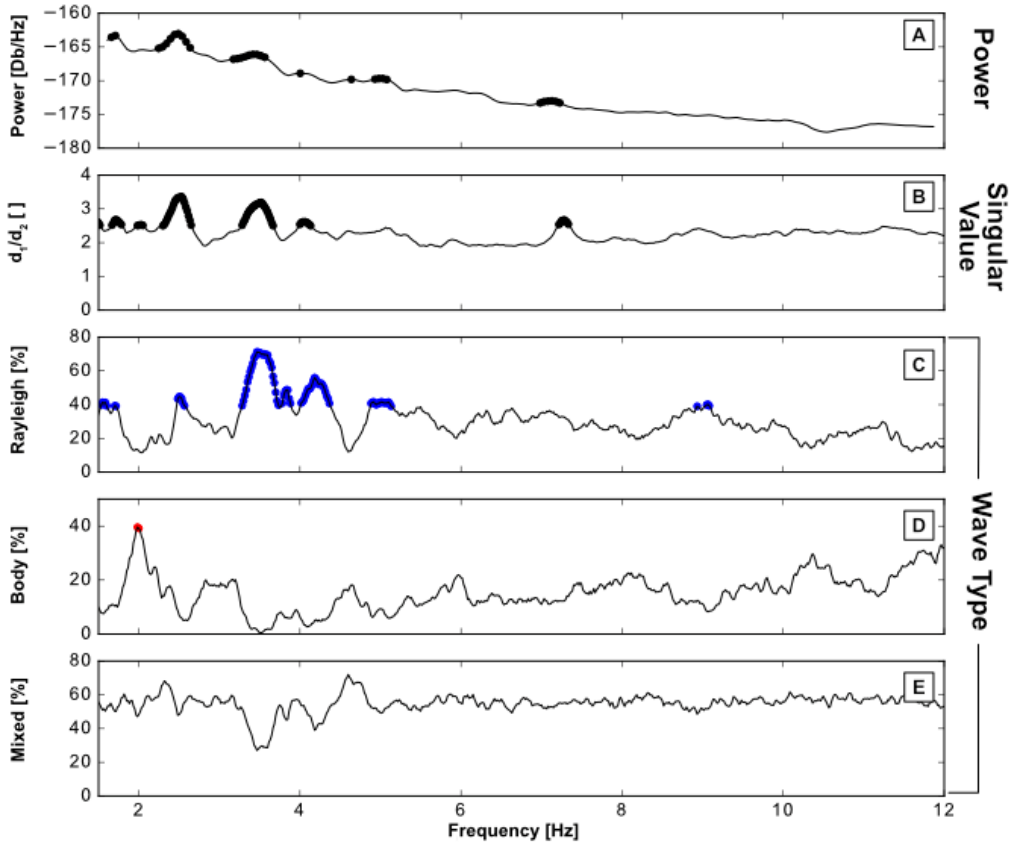

Figure 3.4: Representation of the glaciohydraulic tremor constraints at seismic station RTBD on July 4, 2016 (A) Power peak constraint. The bold lines represent the peaks in power and the thin black line is the smoothed median vertical PSD for July 4th at RTBD. (B) Wave polarization constraint. Bold segments represent wave polarization ratios that exceed 2.5 (C- E) Wave type constraint with each frame representing one of three categories: (C) Rayleigh waves (D) body waves (E) mixed waves. The threshold value for peaks in Rayleigh waves and body waves is 39% and the threshold value for mixed waves is 96%. The colored lines represent the frequencies that experience peaks of a given wave type. The frequencies where all three of these constraints hold true are those that contain locatable glaciohydraulic tremor.

component (as defined by the first, power peak constraint) which allows me to disregard Love waves as they have no vertical motion.

The threshold value for wave type peaks is found by comparing a randomly distributed set of waveforms to the actual waveform distribution. If the calculated wave form percent is 75% greater than what is expected in a randomly distributed sample, then a wave form peak occurs. Again, the threshold (75% in this case) was chosen on a qualitative basis, through repeated comparison between threshold peaks and visually identifiable peaks at the majority of seismic stations. Larger threshold values begin to exclude peaks in wave type while lower thresholds include unexceptional, low percentages. In a randomly distributed system, I expect 22% of the waveforms to be categorized as Rayleigh waves, 22% of the signal to be categorized as body waves, and the remaining 56% of waves to be mixed waves. If threshold values are 75% greater than the expected value, then the threshold percentage for body waves and Rayleigh waves is 39% and the mixed wave threshold is 96% (Fig. 3.4C-E).

3.3- Synthetic testing of frequency dependent polarization analysis

Synthetic waveforms can be used to validate the accuracy of backazimuth estimates produced through frequency dependent polarization analysis. Sine waves

$$W = A\sin(2\pi ft + l) + cN \qquad (12)$$

are used to create synthetic three-channeled seismic signals, with the north and east channel amplitudes used to calculate the expected backazimuth. In equation 12, *A* is the amplitude of the wave, *f* is frequency, *t* is time, *l* is the phase lag, *N* is random, normally distributed noise with a mean of zero and a standard deviation of 1 that is added to the signal, and *c* is a scaling factor that effectively increases the standard deviation of the noise.

A noisy synthetic example of a three component seismic signal is used to show the validity of FDPA

$$Vertical = \sin\left(2\pi 7t + \frac{\pi}{2}\right) + 6N \qquad (13)$$

$$North = \sin(2\pi 7t) + 6N$$

$$East = -\sin(2\pi 7t) + 6N$$

which corresponds to the waveform in figure 3.5A. In this example, the expected backazimuth is 315˚ and the waveform frequency is 7 Hz (Fig. 3.5B), which is where the most significant

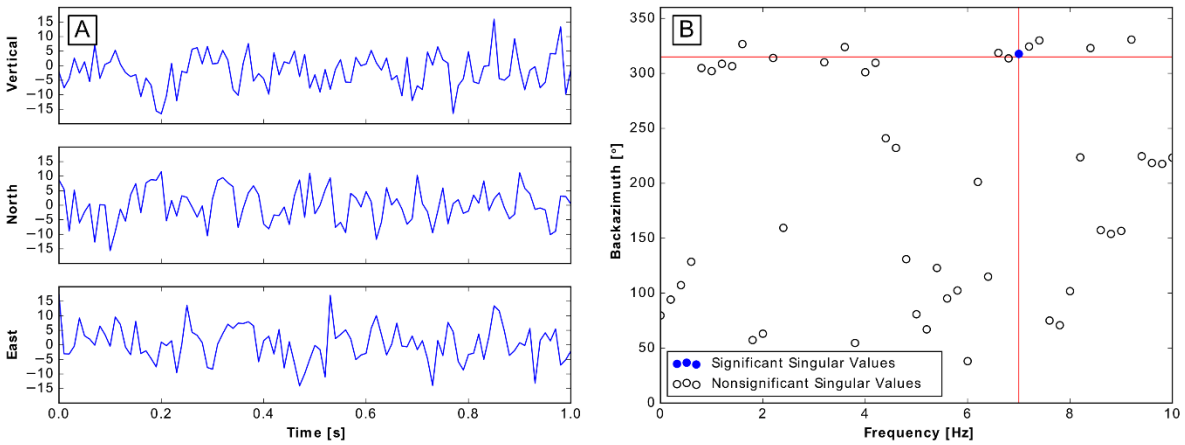

Figure 3.5: An example of synthetic waveforms used to validate the accuracy of backazimuths produced through FDPA (A) Synthetic waveform produced by equation 13, with a frequency of 7 Hz and an expected backazimuth of 315˚. (B) The backazimuth estimate for the synthetic waveform. The expected backazimuth and frequency are represented by the horizontal and vertical red lines respectively. The intersection between these two lines is where the significant backazimuth results (represented by blue dots) are expected to occur. Significance is determined by the singular value ratio.

backazimuth measurements are expected to occur. As defined by the polarization constraint for glaciohydraulic tremor, I consider the backazimuth measurement to be significant if the ratio between the first and second singular value is greater than 2.5.

The location of the significant backazimuth relative to the expected values in figure 3.5B validates that, even in a noisy, synthetic seismic "environment" with a signal to noise ratio of 1:6, frequency-dependent backazimuths can be estimated accurately using the method described above. Signal to noise ratios that are less than 1:6, prevent a significant backazimuth measurement from being identified, which means that the waveform is no longer dominantly polarized. As the signal to noise ratio increases, the accuracy of the backazimuth estimate improves.

3.4- Water input estimations

To analyze the relationship between glaciohydraulic tremor and subglacial water flow, estimates of daily water input to the subglacial water system are needed. I calculate daily melt using a degree day melt model

$$M = \begin{cases} DDF \sum T\Delta t, & T > 0 \\ 0, & T \leq 0 \end{cases} \qquad (14)$$

where T represents the average temperature at a given location over a time span Δt and DDF is the degree day factor which differs depending on snow or ice cover.

I extrapolate air temperature measured at ETIP and TWLV across the glacier surface using an empirically determined lapse rate from differences between temperatures at TWLV and ETIP. A 5m DEM of Taku glacier collected by IfSAR in 2012-2013 [*Fugro EarthData, Inc*] is used and resampled to 25m. The DEM is clipped to Taku glacier's extent from the Randolph Glacier Inventory [*Kienholz et al.*, 2015]. Hole-In-The-Wall Glacier, which branches off Taku glacier to the east (Fig. 2.1), is removed under the assumption that it contributes no melt to the subglacial water system of Taku glacier. The daily median temperatures are extrapolated to all grid cells of the preprocessed DEM

$$T_x = (H_x - H_E) * (\frac{T_W - T_E}{H_W - H_E} + T_E) \quad (15)$$

where *T* represents the temperature, *H* represents the elevation of the grid cell, subscripts *W* and *E* represents weather station TWLV and ETIP respectively, and subscript *x* represents the grid cell of interest. . Due to equipment failure, temperatures at TWLV are estimated after June 28th using adiabatic cooling rate estimates. A clear relationship between temperature differences at ETIP and TWLV and humidity at ETIP allows for an estimate of adiabatic cooling rate as a function of humidity. These adiabatic cooling rates allow for estimates of air temperature distributed across the entire glacier surface during the late summer using temperature and humidity records at ETIP alone.

Degree day factors on Taku glacier and daily snowline elevation are also needed for the degree day melt model. DDF values of Alforbreen Glacier, Sweden were utilized on Taku glacier due to similar latitudes and environments of the two glaciers [*Hock*, 2003]. The DDF value of snow is 4.5 and the DDF value of ice is 6. To determine if a grid cell was snow covered or ice covered on a given day, snow line elevation estimates are calculated. I use clear sky Landsat 7 and 8 images between April and October (5 images) to estimate the location of the snow line. I linearly interpolate the daily snow line elevation for days between measured snow line elevations.

Since glaciohydraulic tremor is produced by water flow past a given location in the subglacial water system, I assume water input lower in elevation than a measurement location does not contribute to the tremor signal. Thus, a separate melt estimate for ETIP, RTBD, and TWLV is needed, since each station sees glaciohydraulic tremor at a different elevation. GIW stations are excluded from the melt estimates considering most of the tremor bands at these

stations point off glacier, signifying that the tremor in not due to subglacial water flow (Section 4.3-4.4). I also assume that ice melt is the only melt that contributes to water input. Although snow melt just above the snowline likely contributes to the subglacial water system, I expect that meltwater either refreezes as it percolates through the snowpack or is otherwise stored in a densifying snowpack in the majority of the accumulation area of Taku glacier [*Pelto et al.*, 2008]. Due to my inability to specify the elevation at which snow melt storage in the snowpack stops, I omit it all together. Estimates of ice melt provide us with a minimum, daily water input into the system and allows us to look at commonalities between the ice melt and tremor. While the true magnitude of subglacial discharge may differ from my estimate, I expect that the temporal fluctuations in subglacial discharge are captured by my model.

To complete the estimate of water input into the subglacial water system, I also include rain events into the model. For days where precipitation fell, I assume that the rain totals that are recorded at ETIP represent the amount of rain that fell over each 25m DEM grid cell that has an air temperature above 0˚C. Consistent with my handling of snow/ice melt, I exclude water inputs from precipitation that falls on grid cells above the snowline elevation (Fig. 5.2).

4. Results

4.1- Frequencies of glaciohydraulic tremor

Estimates of tremor frequency and wave type for all seismometers on Taku glacier using the three constraints outlined in section 3.2, reveal multiple distinct frequency bands of polarized glaciohydraulic tremor, each with a defining wave type. Two distinct bands of sustained, polarized, Rayleigh wave glaciohydraulic tremor exist at RTBD, one between 2.35 - 2.7 Hz and the other between 3.2 - 3.7 Hz (Fig. 4.1A). Glaciohydraulic tremor at ETIP reveals a more complex signal composition, with multiple bands of polarized Rayleigh wave, body wave, and mixed wave signals (Fig. 4.1B). Some of these tremor bands exhibit frequency gliding, as highlighted by the upper left-hand box in figure 4.1B, in which the signal decreases in frequency as the melt season progresses. ETIP also experiences tremor signals that alternate between wave types throughout the melt season, which can be seen in the lower right-hand box in figure 4.1B. Tremor onset dates vary between stations, with polarized, Rayleigh wave glaciohydraulic tremor beginning on June 1st at ETIP, June 21st at RTBD, and August 22nd at TWLV.

Each seismic station exhibits different frequencies of polarized, Rayleigh wave glaciohydraulic tremor (Fig. 4.2). Frequency distributions of other wave types are not shown here due to my interest in Rayleigh wave glaciohydraulic tremor. All polarized Rayleigh wave signals are contained between 1.5 and 10 Hz which is consistent with the frequencies of water-produced tremor reported in current literature [*Burtin et al.*, 2008; *Schmandt et al.*, 2013;

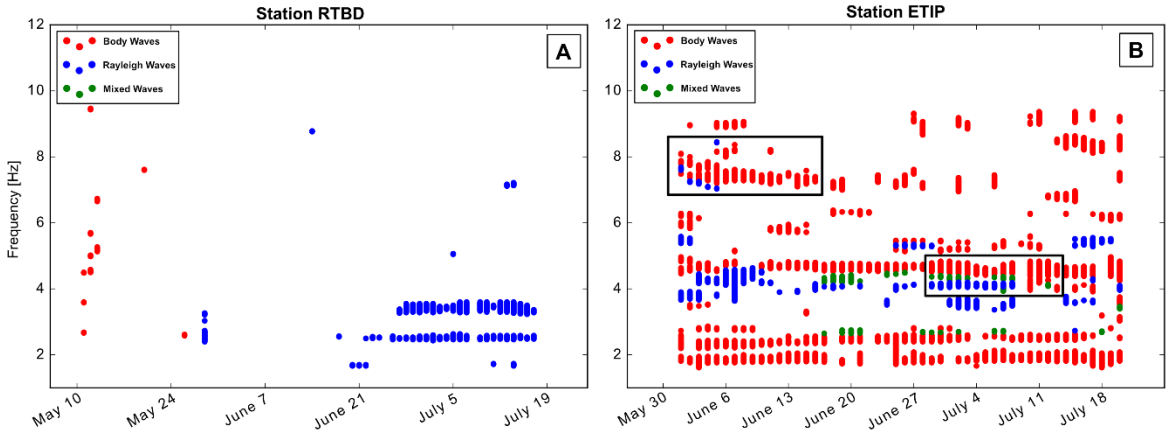

Figure 4.1: Frequency bands of polarized glaciohydraulic tremor and their defining wave type throughout the melt season. (A) Station RTBD with two distinct bands of polarized Rayleigh wave glaciohydraulic tremor (B) Station ETIP with bands of Rayleigh wave, body wave, and mixed wave tremor. Two boxed regions in (B) exist: The top left-hand box highlights frequency gliding in the seismic signal and bottom right hand box highlights changes in the dominate wave type for a given frequency.

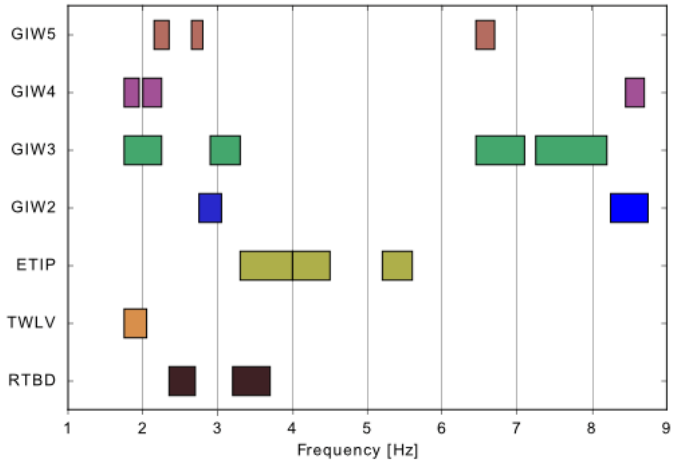

Figure 4.2: Polarized, Rayleigh wave glaciohydraulic tremor frequencies for seismic station around Taku glacier. The y-axis represents the 7 seismometers and each box spans the frequency range of a polarized, Rayleigh wave glaciohydraulic tremor band.

Bartholomaus et al., 2015]. All seismic stations recorded Rayleigh wave tremor below 4 Hz with only GIW3, GIW4, and GIW5, at the glacier terminus recording tremor above 8 Hz. The frequency ranges of polarized, Rayleigh wave tremor vary among stations, however all the tremor bands span less than a single Hertz.

4.2- Backazimuths of glaciohydraulic tremor

Backazimuth probabilities (Fig. 4.3) allow us to estimate the source location of polarized, Rayleigh wave glaciohydraulic tremor. At RTBD, both Rayleigh wave glaciohydraulic tremor bands (Fig. 4.1A) come from a southeastwardly direction, with the highest probability backazimuths for all frequencies around 135˚. The probability range, as specified by the color ramp in figure 4.3, is similar at stations RTBD and TWLV over the duration of the record, both having an average maximum probability within tremor bands of 0.16. ETIP exhibits much higher probability values with an average maximum probability of 0.52. Polarized, Rayleigh wave glaciohydraulic tremor source locations at seismometers around Taku glacier can be visualized in figure 4.4. Glaciohydraulic tremor sources at ETIP, RTBD, and TWLV (Fig. 4.4A) radiate from Taku Glacier with tremor bands at a given station coming from similar directions. However, more scatter in the source locations at GIW stations exist (Fig. 4.4B-C) with backazimuths coming from multiple directions.

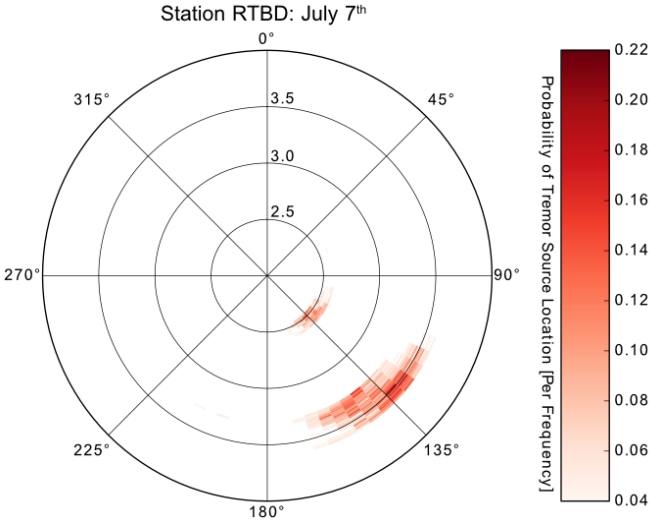

Figure 4.3: Probability of backazimuth locations for polarized, Rayleigh wave glaciohydraulic tremor signals at station RTBD on July 7th. Backazimuths are defined clockwise from north (0˚). Radii on the polar plot denote frequencies between 2 and 4 Hz, with increasing radii signifying an increase in frequency values. The color ramp depicts the probability of a waveform's source location with darker reds representing higher probabilities.

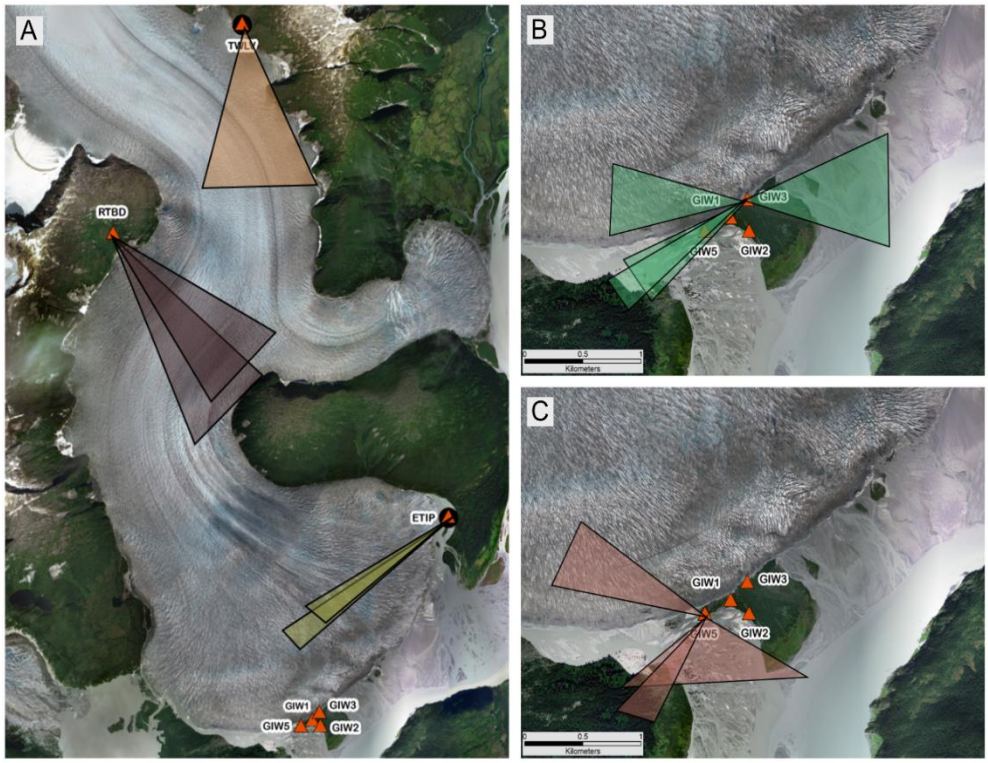

Figure 4.4: Map of backazimuth locations at stations on Taku glacier with ETIP, RTBD, GIW3, and GIW5 representing July 4th, and TWLV representing September 14th. Each triangle represents a different polarized, Rayleigh wave glaciohydraulic tremor frequency band, with the width of a triangle representing the range of backazimuth estimates between the 25th and 75th percentile of measurements on a given day. The length of a triangle is arbitrary. (A) Backazimuth estimates at TWLV, RTBD, and ETIP (B) GIW3 backazimuth estimates (C) GIW5 backazimuth estimates.

4.3- Temporal variations in glaciohydraulic tremor

Time lapse allows us to visualize significant changes to source probabilities of polarized, Rayleigh wave glaciohydraulic tremor as well as track frequency fluctuations throughout time. Video 1 shows changes in the frequency and probability of glaciohydraulic tremor source locations over the melt season by stitching together polar plots (Fig. 4.2) of consecutive days. Video 1 shows slight day to day fluctuations in probabilities and frequencies of tremor at RTBD over a two-week period, however no obvious, monotonic changes occur. Backazimuth estimates remain near 135˚.

I visualize the changes in polarized, Rayleigh wave glaciohydraulic tremor backazimuths, within specific frequency bands, using box plots that span the temporal scale of the glaciohydraulic tremor signals (Fig. 4.5). The backazimuths at ETIP (Fig. 4.5C-D) cover a smaller range of values between the 25th and 75th percentile than those at RTBD (Fig. 4.5A-B), with the average range of backazimuth measurements at ETIP being between 6˚-8˚

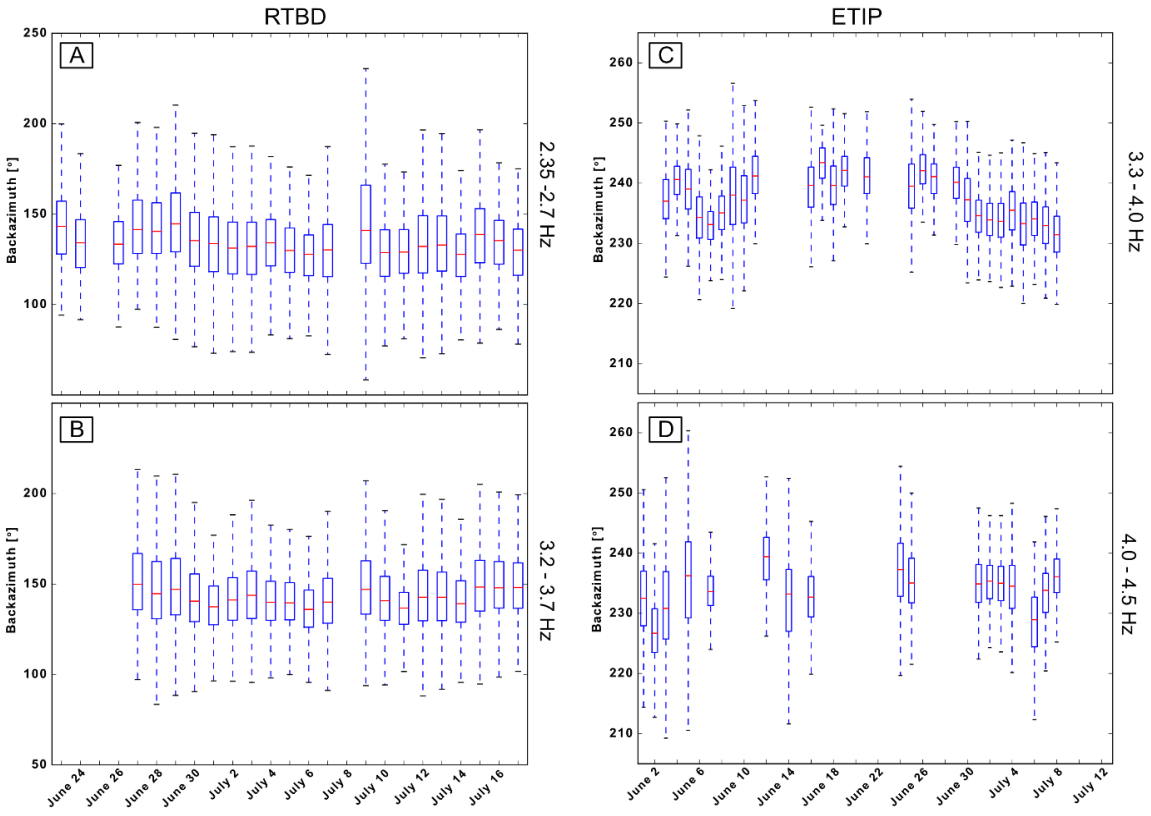

Figure 4.5: Box plots of backazimuth locations on a daily time scale for different polarized, Rayleigh wave glaciohydraulic tremor frequencies. The red line represents the median value of backazimuth estimates and the 25th and 75th percentile represents the bounding edges of each box (A) 2.35-2.7 Hz at RTBD (B) 3.2-3.7 Hz at RTBD (C) 3.3-4.0 Hz at ETIP (D) 4.0-4.5 Hz at ETIP.

and the average range of backazimuths at RTBD being 25˚-28˚. Both RTBD and ETIP experience migration in median backazimuth estimates over the melt season with the median backazimuth at RTBD fluctuating by 14˚-21˚ and 13˚-14˚ at ETIP. While these fluctuations in backazimuths are similar at both stations, I have more confidence in the backazimuth changes at ETIP because they are nearly double the interquartile range of measurements, while median backazimuth changes at RTBD do not exceed the backazimuth interquartile range (25˚-28˚) observed in a single day. Station TWLV is excluded from this analysis due to the lack of sustained tremor signal which provides very few days of polarized, Rayleigh wave glaciohydraulic tremor. Many of the tremor sources identified by the GIW stations do not propagate from the glacier, so I exclude them from this analysis.

5. Discussion

5.1- Spatial organization of the subglacial water system

The spatial organization of subglacial conduits is one of the many unknowns in glacial hydrology. Glaciohydraulic tremor daily median power comparisons (Fig. 5.1) and time series analysis (Fig. 4.5) provide insight into this spatial organization on Taku glacier. Figure 5.1B and 5.1C show the relationship between daily median power estimates of tremor bands at ETIP, calculated by taking the median of all power values in a given frequency range. I find that, while these powers are correlated, they experience scatter during the latter part of the melt season and that power within the 4.0-4.5 Hz band is nearly 10 times higher than power in other tremor bands at ETIP. These findings reveal complexity in the seismic sources of tremor which may be explained by multi-conduit flow with varying water fluxes through individual conduits. In contrast with those at ETIP, the median power of different glaciohydraulic tremor bands at RTBD are nearly perfectly correlated ($R^2 = 0.98$, Fig. 5.1A). This correlation may be explained by tremor bands being emitted from the same source within a single subglacial conduit.

Due to different water flow patterns observed at ETIP and RTBD, I suggest that subglacial water system organization is strongly dependent on the lateral hydraulic potential gradient of a glacier's bed. Nolan et al. (1995) and Motyka et al. (2006) both use radio echo sounding to map cross sections of Taku Glacier, which show a steep lateral hydraulic gradient of about 2,000 Pa/m at locations near RTBD and nearly flat lateral gradients within 5.5 km of the terminus [*Nolan et al*., 1995]. Steep, lateral potential gradients tend to produce channelized flow that is constrained to the deepest portion of the valley floor, while flow on a flat surface can spread out across the landscape in delta-like flow patterns [*Shreve*, 1972]. This envisioned, distributary water flow mirrors the broadening, distributary ice flow of the glacier terminus. This correlation between lateral potential gradients and subglacial conduit organization allows for the prediction of subglacial water flow patterns at locations where time series analysis and tremor power comparisons are not possible, such as station TWLV. Since areas around TWLV have cross sections like those in proximity to RTBD, I predict that TWLV records tremor produced by single conduit flow.

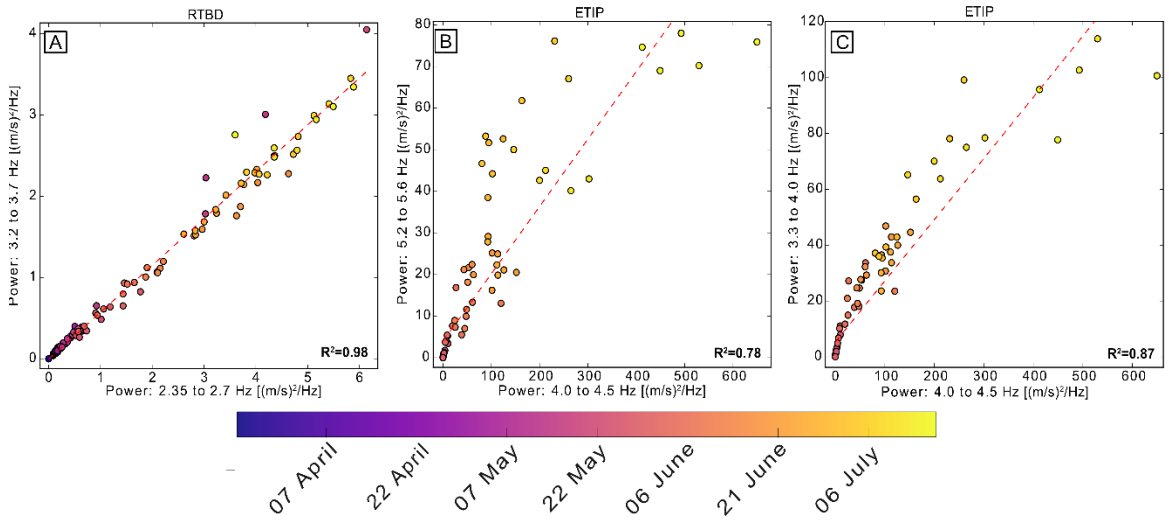

Figure 5.1: Temporal changes in median power correlations between different frequency bands of glaciohydraulic tremor. Each axis represents the median power of a given frequency band and each observation represents the daily median power with the color ramp representing the temporal progression of the 2016 melt season. The red dotted line represents the line of best fit and the corresponding R^2 value located in the bottom right hand corner of each frame (A) Station RTBD with power scaled by 10^{-17}; (B and C) Station ETIP with power scaled by 10^{-15}.

5.2- Temporal scales of conduit evolution

The temporal scales of subglacial conduit evolution are another broad unknown in glacial hydrology. While glaciohydraulic tremor power broadly follows water inputs, locatable glaciohydraulic tremor requires sustained water input rather than transient melt or rain events (Fig. 5.2). Transient water input events, such as rain or high melt days, do not occur on the days of polarized, Rayleigh wave glaciohydraulic tremor initiation but do occur throughout the data collection period, both prior to and after tremor initiation. This implies that seasonally-sustained subglacial conduits producing locatable glaciohydraulic tremor do not form during these transient events. On the days of polarized, Rayleigh wave tremor initiation, the snow-ice interface on Taku glacier is 200-300 m above the tremor elevation (Fig. 5.2), indicating that tremor initiation doesn't occur until the snow line has significantly retreated past the elevation at which tremor is recorded and sustained ice above the seismic station occurs. I find that at least 20 days of sustained ice melt above the elevation of the seismic stations occurs prior to tremor initiation at all stations. In the week prior to the start of sustained tremor at both ETIP and RTBD, subglacial water flow rates exceeds 4 m^3/s, while TWLV experience much higher sustained volumetric water flow rates of 18 m^3/s in the week prior to tremor onset.

Figure 5.2 also allows for the comparison of polarized, Rayleigh wave glaciohydraulic tremor initiation and the median power of glaciohydraulic tremor frequencies. Seismic power consistently increases prior to tremor initiation at both ETIP and RTBD, however consistent median power with multiday-power peaks occur prior to the initiation of sustained polarized, Rayleigh wave glaciohydraulic tremor at TWLV. The multi-day power peaks that occur in late July at TWLV (Fig. 5.2) seem to be associated with two late July rain events, thus this power response is presumably produced by subglacial water flow even though tremor doesn't begin at TWLV for another month. This discrepancy leads to the re-examination of glaciohydraulic tremor constraints proposed in section 3.2 for a potential limiting factor of tremor frequencies. While high-powered Rayleigh wave seismic signals are present at TWLV prior to August 22nd (the date of sustained polarized, Rayleigh wave glaciohydraulic tremor initiation), my polarization metric remains below the threshold ratio of 2.5 prior to this date. Thus, particle motion at TWLV, while exhibiting Rayleigh wave elliptical motion and high amplitudes, is not concentrated within a single plane of motion. From this finding I conclude that waveforms at TWLV are less polarized than those at ETIP and RTBD. Sustained, non-polarized seismic tremor that gradually becomes polarized, which occurs at TWLV, may

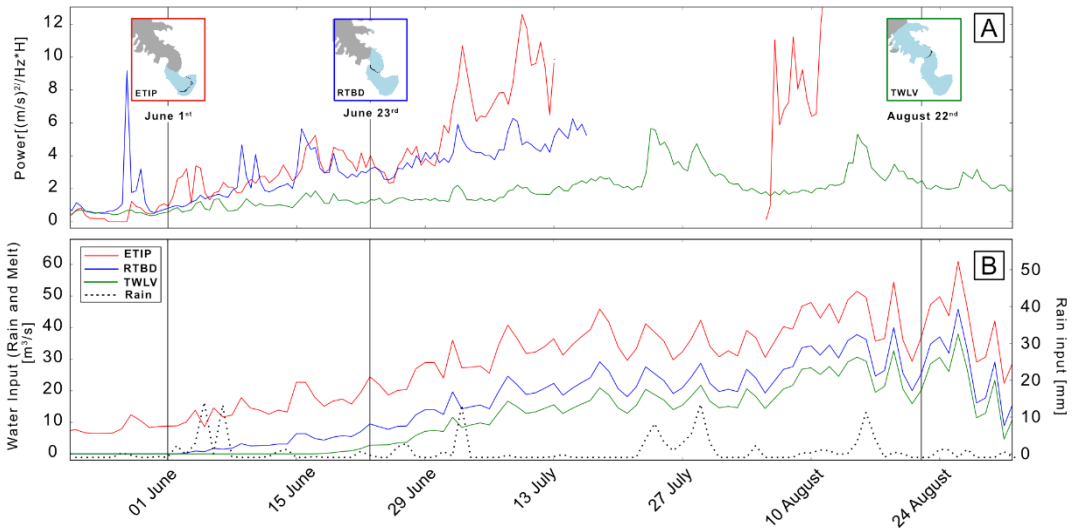

Figure 5.2: Comparison between sustained, polarized, Rayleigh wave glaciohydraulic tremor initiation, snow-ice interface elevation, median seismic power, and water input and rain events. (A) Daily median power at three seismic stations, ETIP, RTBD, and TWLV for given frequency ranges of tremor: 3.3-4.0Hz for ETIP, 2.35-2.70 Hz for RTBD and 1.75-2.05 Hz for TWLV. Power at RTBD and TWLV are scaled by 10^{-17} and ETIP power is scaled by 10^{-14} (Map inserts) Snow-ice interface elevation in relation to tremor elevation on the date of sustained tremor initiation. Gray represents snow cover, blue is ice cover and the black line represents the average elevation of tremor. The date under each map insert is the day sustained polarized Rayleigh wave glaciohydraulic tremor began. (B) Ice melt and rain inputs into the subglacial water system. Colored lines depict the sum of melt and rain events over the elevations above the identified seismic station.

identify a distributed water system with high water fluxes that progressively forms into a single conduit as the melt season progresses.

Sustained water input prior to the initiation of polarized, Rayleigh wave glaciohydraulic tremor as well as the lack of correlation between transient water input events and tremor onset leads to the conclusion that some volume of sustained water input is essential for conduit formation. This finding is supported by those presented in Schoof [2010]. I suggest that volumetric flow rates must exceed 4 m^3/s in order for sustained, polarized, Rayleigh wave glaciohydraulic tremor to be produced. To identify a more precise threshold of subglacial discharge, site specific degree day factors should be calculated on Taku glacier and better monitoring of snow depths and snowline retreat is needed.

Another unknown in subglacial hydrology is the temporal scale of subglacial conduit migration which may influence local glacier dynamics. In low hydraulic gradient areas where I suggest multi-conduit flow exists due to scatter in median power comparisons (Section 5.1), source locations experience multiday shifts (Fig. 4.5C-D). I hypothesize that this phenomenon occurs due to water shifting between neighboring conduits or up- and down-conduit motion of obstructions that focus the production of glaciohydraulic tremor. To explore this hypothesis, I analyze the power relationships between tremor bands of ETIP (Fig. 5.1) in greater detail (Fig. 5.3). Figure 5.3 reveals multiday clusters of tremor power indicated by boxes 1-3, with box 1 spanning June 11^{th}-15^{th}, box 2 spanning June 16^{th} -22^{nd}, and box 3 spanning June 26^{th}- 30^{th}. I assume that each band of tremor frequencies is produced in a unique conduit, thus the x-axis represents power produced in what I term conduit A and the y- axis represents power produced in what I refer to as conduit B. As time progresses from box 1 to box 2 within figure 5.3, I see a transition in which power increases in conduit A (indicating an increase in water flow), while water flux in conduit B remains stable. This increase in power is followed by consecutive days of stable water flow patterns, with a steady ratio between the conduits (indicated by the clustering of power). Following 7 days of steady water flow, another relatively rapid transition occurs from box 2 to box 3. I interpret this as an increase in water flow within conduit B, while flow in conduit A remains steady, followed again by 5 days of consistent water flow patterns. Median power clusters between these tremor bands last between 4-7 days before switching to a new water flow arrangement. Between 3.3-4.0 Hz and 4.0-4.5 Hz frequency bands at ETIP (not shown), median power clusters do not

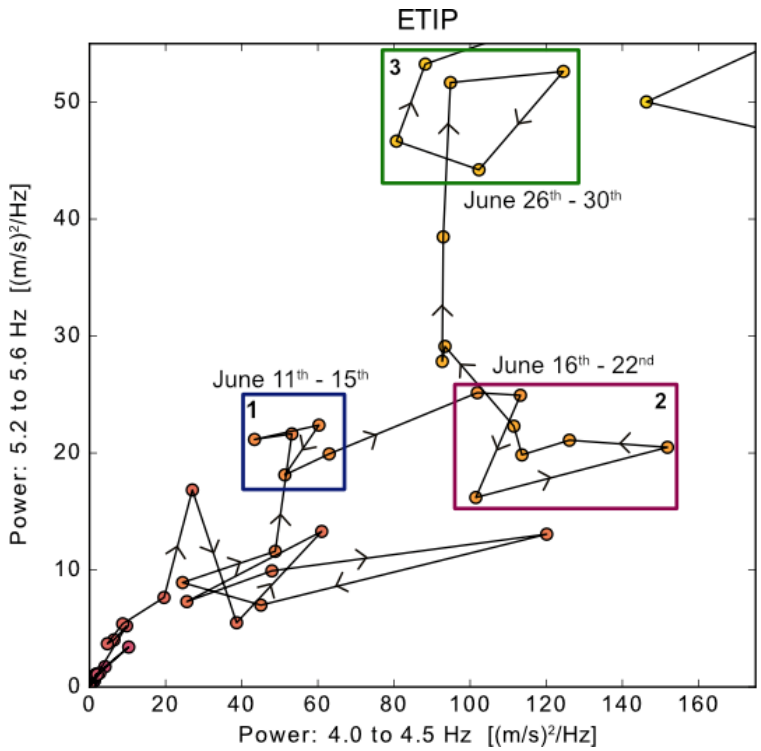

Figure 5.3: Multi-day clustering of median seismic power (a subset from figure 5.1). Boxes enclose consecutive days with similar power between the two frequency bands, with the dates representing the days where clustering occurs. Power of different glaciohydraulic frequency bands at ETIP, represented on each axis. Each frequency band is representative of a different conduit, with the 4.0-4.5 Hz band classified as conduit A and 5.2-5.6 Hz representing conduit B. Arrows indicate how the power is changing over consecutive days.

exceed 3 days, which we interpret to reflect greater dynamism within the subglacial hydrologic system. Backazimuth estimates at ETIP (Fig. 4.5C-D) also experience 3-4 day clusters, which is similar to the duration of power clusters. I hypothesize that the changes in the water flux within different conduits may be due to erosion and deposition of sediment within a conduit which can change the location of focused tremor production, changes to water input in individual conduits (i.e., if one subglacial conduit taps a larger contributing glacier surface area through connection and disruption of tributary conduits), or slight changes in conduit geometry. These results reveal that the subglacial hydrologic system in low lateral gradient areas on Taku glacier evolves through abrupt jumps between quasi-stable configurations that last between 3-7 days.

5.3- Water input and tremor power relationships

There is an apparent relationship between tremor and subglacial water flow, which implies that discharge may be inferred from tremor. I find that different relationships between

water input and tremor power exist for all polarized, Rayleigh wave glaciohydraulic tremor bands with higher frequency signals tending to have lower power for a given discharge than lower frequency tremor bands, with the exception of the 4.0-4.5 Hz band at ETIP (Fig. 5.4). This may be explained by the fact that higher frequency seismic signals attenuate faster than lower frequency signals [*Battaglia and Aki*, 2003]. The power decay anomaly within the 4.0-4.5 Hz band may be explained by the output stream that flows between ETIP and Taku glacier. This tremor band switches from Rayleigh wave dominant to body wave dominant signals throughout the melt season, which may indicate that the highest amplitude signal in the 4.0-4.5 Hz range switches to a source closer to the seismic station (Fig. 4.1) (Section 5.4).

To explore the frequency dependent attenuation hypothesis, I use the amplitude decay model outlined in Battaglia and Aki [2003]. This model, modified to consider power rather than amplitude decay, holds that

$$P(f) = \frac{P_0}{r^n} e^{-\alpha r}, \tag{16}$$

in which $P(f)$ represents the seismic power of frequency f recorded at a seismic station a distance r from the source, P_0 is the source seismic power, and n is the geometrical spreading rate. I will test the scenario that the original seismic power, P_0, and the distance between the source and station, r, remains the same between all frequency bands, under the assumption that all power bands are produced at the same location. The geometrical spreading rate, n, is not dependent on frequency; thus, this is held fixed throughout the analysis.

The anelastic attenuation coefficient of waves with frequency f,

$$\alpha = \frac{\pi f}{Q\beta} \tag{17}$$

is found using the seismic quality factor, Q, and the seismic wave velocity, β, which are dictated by the properties of the medium in which the wave moves. I utilize the seismic quality factor and wave velocity from the Greenland Ice Sheet as determined by Roosli et. al [2014]. While Q is location dependent, $Q = 4$ was found in a glacial setting and at a similar frequency range to my study. Surface wave velocity through glacier ice is estimated to be 1.65 km/s [*Mikesell et al.*, 2012; *Röösli et al.*, 2014].

To analyze the ratio of power decay between different tremor frequencies at a given station, the power decay ratio T

$$T = \ln\big(P(f_x)\big) - \ln\Big(P\big(f_y\big)\Big) = \frac{\pi}{Q\beta}(f_y - f_x) \tag{18}$$

is found from the division of power levels recorded in frequencies *x* and *y* (Eq. 16), where the frequency is represented by the median frequency of a given tremor band.

The theoretical power decay ratio between the tremor frequency bands of 2.35-2.7 Hz and 3.2-3.7 Hz at RTBD is 0.44 while the actual average decay ratio is 0.58. At ETIP I find a much larger range between the theoretical and actual decay ratios for the frequency bands of 3.3-4.0 Hz and 5.2-5.6 Hz, with $T_{theoretical}$ = 0.83 and T_{actual} = 0.43. The powers in the intermediate frequency range at ETIP, near 4.3 Hz, are clearly following a different relationship with water inputs and are not analyzed using the power decay model. Some of the discrepancy between the theoretical and actual values at both stations can be explained based on uncertainty associated with the seismic quality factor. Quality factors for ice range from Q=35 for 20 Hz signals on the Greenland Ice Sheet [*Jones et al.*, 2013] to Q=3.4 for low frequency events on the Cotopaxi volcano ice cap [*Metaxian et al.*, 2003]. Differences between the theoretical and actual ratio decreases as lower Q values are chosen. For example, if power decay ratio at RTBD is estimated using Q=3.4 instead of Q=4, the difference between the theoretical and actual ratio decreases from 0.14 to 0.06. This suggests that while my selection of the Q value is able to account for some of the discrepancy in the power decay ratios, my assumption my not entirely hold. Thus, seismic power generated at the source may differ slightly between frequency bands or the two frequency bands may originate at slightly different distances from the station.

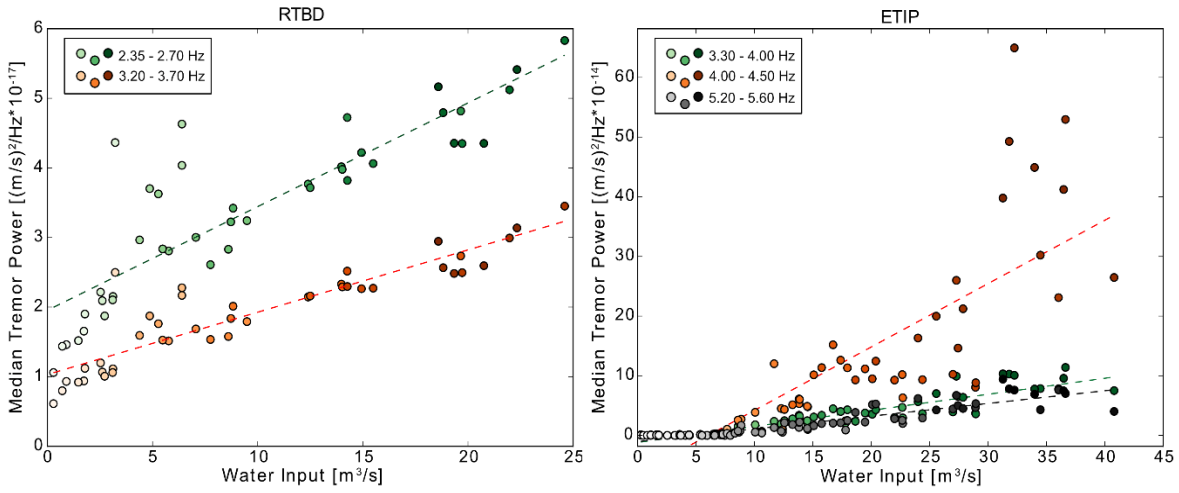

Figure 5.4: Relationship between water input and the median tremor power at (A) RTBD and (B) ETIP. Each point represents one day, with different color ramps representing different glaciohydraulic tremor frequency bands. Lighter hues in the color ramp represent days early in the melt season (May) and darker hues represent mid melt season (July).

Based on my power decay ratio analysis, I suggest that, at station RTBD (Fig. 5.4A) where single conduit flow most likely exists, the differing relationship between the two tremor bands is primarily due to faster power decay in higher frequency signals. While the different frequency bands may reflect different source processes or source geometry, it is also possible that these sources are at the same location, emitting the same power but in distinct frequency bands. At ETIP (Fig. 5.4B), where median power comparisons (Fig. 5.1) are consistent with multi-conduit flow, the differing relationship between water input and tremor power for frequency bands 3.3-4.0 Hz and 5.2-5.6 Hz may be due to different water fluxes through a series of conduits, instead of being produced from the same source. The large discrepancy in the theoretical and actual power decay ratios at ETIP suggests that my assumption of same source location distance may be incorrect at ETIP.

The relationship between power and water input at ETIP also falls within the relationship theorized by Gimbert et al. [2016]. Gimbert et al. [2016] suggests that power from subglacial water flow (P_w) and water discharge (Q) relationships fall between $P_w \propto Q^{\frac{5}{4}}$ and $P_w \propto Q^{\frac{14}{3}}$. Power and water input at ETIP more closely follows the $P_w \propto Q^{\frac{5}{4}}$ relationship (Fig. 5.4B) signifying that power scales with water flow at a constant pressure gradient, in which variations in discharge are accommodated by a conduit with varying hydraulic radius [*Gimbert et al.*, 2016] . Seismic power and water input relationships at RTBD exhibit a linear, not a power relationship, thus the theorized power-discharge relationship of Gimbert et al. [2016] does not model tremor bands at RTBD well.

5.4- Wave composition of glaciohydraulic tremor

This study also provides new seismological insight into the glaciohydraulic tremor signals themselves. I find that glaciohydraulic tremor consists of multiple wave types (Rayleigh waves, body waves, and a mixture of the two) (Fig. 4.1). This finding from Taku Glacier contradicts the common assumption that near-surface tremor signals produced by rivers are dominated by Rayleigh waves [e.g., *Tsai et al*., 2012; *Gimbert et al*., 2014]. While this assumption may hold true in terrestrial rivers, it is not universally true at Taku Glacier.

I hypothesize that the dominant wave type of glaciohydraulic tremor is dictated by the proximity of a seismic station to the source, with sources close to seismic stations being

predominantly composed of body waves and further stations largely recording Rayleigh waves. Body wave power attenuates faster than surface wave power, with the body wave geometrical spreading rate equal to 2 and the surface wave geometrical spreading rate equal to 1. Thus, if body waves dominate a glaciohydraulic tremor frequency, the body waves may not have significantly attenuated, suggesting the source is closer to the station than Rayleigh wave-dominated frequencies.

The distance between a seismic station and tremor source also dictates if a seismic wave has had sufficient travel distance to produce the constructive interference between P and SV waves at the earth surface necessary to generate Rayleigh waves. Near-field sources, which I define as sources within 1 wavelength of the seismometer, are not able to form defined Rayleigh waves due to incomplete formation of P or SV waves. If I assume seismic wave velocities of 1.65 km/s (appropriate for Rayleigh waves) within the 1.5- 10 Hz range [*Mikesell et al.*, 2012; *Röösli et al.*, 2014], wavelengths (and the threshold for near field sources) are between 0.17-1.1 km, with longer wavelengths associated with lower frequencies. At ETIP, which shows prominent bands of body wave tremor (Fig. 4.1B), there are both near field glacial and terrestrial river sources that may lead to distinct body wave bands. However, at RTBD, where subglacial water most likely flows at the center of the glacier where the lateral gradient is the steepest, the tremor source is about 2.3 km away from the seismic station, which is greater than the maximum near field source estimate. This provides a possible explanation as to why there are no body wave tremor bands at RTBD (Fig. 4.1A).

5.5- Frequency structure and propagation of Rayleigh wave glaciohydraulic tremor

While there are power increases across a broad range of frequencies on Taku glacier (Fig. 3.2), the strongest power increases composed of polarized Rayleigh waves fall between 1.5 - 10 Hz which is consistent with the findings of Bartholomaus et al. [2015] on Yahtse, Mendenhall, and Columbia Glaciers, and Jakobshavn Isbræ, as well as the tremor frequencies produced by terrestrial rivers [*Burtin et al.*, 2008; *Tsai et al.*, 2012; *Schmandt et al.*, 2013, 2017; *Gimbert et al.*, 2014]. Like the power density spectra in Burtin et al. [2008] and Schmandt et al. [2013], glaciohydraulic tremor exhibits multiple distinct power peaks within this 1.5-10 Hz range. The quantity and frequency ranges of polarized, Rayleigh wave glaciohydraulic tremor power peaks are not consistent between seismic stations (Fig. 4.2),

thus there are no clear, diagnostic seismic signatures of glaciohydraulic tremor at Taku Glacier.

A previously unreported feature of glaciohydraulic tremor is that different frequency bands propagate from the same source direction, as seen in figures 9 and 10. Two different hypothesis may explain this phenomenon: turbulent eddies and subglacial water flow through neighboring conduits. Different sized obstacles in close proximity to one another within a subglacial conduit may produce eddies that emit distinct frequency signatures, where large obstacles produce a broad range of eddy sizes while smaller obstacles only initiate small eddies [*Kolmogorov*, 1941]. This difference in eddy sizes may cause distinct frequency bands to radiate from the same source location. In low hydraulic gradient areas, such as ETIP, where I believe multi-conduits flow occurs, water flowing through neighboring conduits may lead to seismic tremor propagating from the same source direction.

The propagation distance of polarized, Rayleigh wave glaciohydraulic tremor can be determined from the varying dates of tremor initiation between seismic stations on Taku glacier (Fig. 5.2). The tremor signal that started at ETIP on June 1st somewhere near the terminus is not recorded by either RTBD or TWLV which signifies that these signals on Taku glacier can only be detected locally. This same phenomenon occurs between RTBD and TWLV, with the tremor at RTBD not recorded by station TWLV. If I assume the polarized, Rayleigh wave glaciohydraulic tremor signal recorded at RTBD comes from the center of the glacier to the southeast of RTBD (Fig. 4.4), the signal can travel 2.3 km to RTBD but not 5.7 km to TWLV. Thus, polarized, Rayleigh wave glaciohydraulic tremor at Taku Glacier can be recorded from 2.3 - 5.7 km away from the source during mid-summer.

6. Conclusion

This study provides new insight into the organization of Taku Glacier's subglacial water system as well as the time scales of conduit evolution and migration. I find that single conduit and multi-conduit flow can be detected through time series analysis, tremor power comparisons, and water input-power relationships, and that flow patterns depend on the lateral potential gradient of the glaciers bed. Tremor signals produced in low, lateral potential gradient areas experience abrupt jumps between quasi-stable configurations that last between 3-7 days which I hypothesize is due to water influx changes between neighboring conduits. Tremor produced in higher lateral potential gradient areas remains relatively stationary throughout the melt season. I also suggest that at least 4 m^3/s of sustained water input into the subglacial water system is needed to record polarized, Rayleigh wave glaciohydraulic tremor at Taku Glacier. Once formed, these conduits appear stable for the remainder of the summer, at least through mid-July at stations ETIP and RTBD and through early September at TWLV. I also show that the relationship between tremor power and subglacial water flow is dependent on the frequency of tremor, with high frequencies potentially affected by greater attenuation rates.

My study has also revealed previously unreported qualities of glaciohydraulic tremor wave composition, propagation, and frequency structure, which has not been explored in previous literature. I reveal that glaciohydraulic tremor is composed of multiple wave types (Rayleigh waves, body waves, and mixed waves) which contradicts the terrestrial river assumption that all tremor signals are dominated by Rayleigh waves [*Tsai et al.*, 2012; *Gimbert et al.*, 2014]. I also conclude that polarized, Rayleigh wave glaciohydraulic tremor propagates no further than 2.3-5.7 km during mid-summer. Glaciohydraulic tremor on Taku Glacier also shows no clear, diagnostic spectral signatures, but often produces multiple distinct peaks in glaciohydraulic tremor seismic power that propagate from the same source direction.

Seismology provides a continuous method to monitor subglacial water flow and the evolution of the subglacial water system. Future research involving geographical positioning systems (GPS), ground penetrating radar (GPR), and a denser network of weather and melt observations may lead to more precise subglacial conduit locations, new techniques for locating sources of body wave glaciohydraulic tremor, and a better quantification of the

relationship between water input and glaciohydraulic tremor power. Seismology can be used to monitor spatiotemporal changes within the subglacial water system and, if used in tandem with other observational methods, may lead to a yet deeper understanding of the relationship between subglacial water flow and glacier dynamics.

References

Bartholomaus, T. C., R. S. Anderson, and S. P. Anderson (2008), Response of glacier basal motion to transient water storage, *Nat. Geosci.*, *1*(1), 33–37, doi:10.1038/ngeo.2007.52.

Bartholomaus, T. C., J. M. Amundson, J. I. Walter, S. O'Neel, M. E. West, and C. F. Larsen (2015), Sublacial discharge at tidewater glaciers revealed by seismic tremor, *Geophys. Res. Lett.*, 6391–6390, doi:10.1002/2015GL064590.Received.

Bartholomew, I., P. Nienow, D. Mair, A. Hubbard, M. A. King, and A. Sole (2010), Seasonal evolution of subglacial drainage and acceleration in a Greenland outlet glacier, *Nat. Geosci.*, *3*(6), 408–411, doi:10.1038/ngeo863.

Battaglia, J., and K. Aki (2003), Location of seismic events and eruptive fissures on the Piton de la Fournaise volcano using seismic amplitudes, *J. Geophys. Res.*, *108*, doi:10.1029/2002JB002193.

Burtin, A., L. Bollinger, J. Vergne, R. Cattin, and J. L. Nábělek (2008), Spectral analysis of seismic noise induced by rivers: A new tool to monitor spatiotemporal changes in stream hydrodynamics, *J. Geophys. Res. Solid Earth*, *113*(5), 1–14, doi:10.1029/2007JB005034.

Chu, V. W. (2014), Greenland ice sheet hydrology: A review, *Prog. Phys. Geogr.*, *38*(1), 19–54, doi:10.1177/0309133313507075.

Cowton, T., P. Nienow, A. Sole, J. Wadham, G. Lis, I. Bartholomew, D. Mair, and D. Chandler (2013), Evolution of drainage system morphology at a land-terminating Greenlandic outlet glacier, *J. Geophys. Res. Earth Surf.*, *118*(1), 29–41, doi:10.1029/2012JF002540.

Fountain, A. G., and J. S. Walder (1998), Water flow through temperate glaciers, *Rev. Geophys.*, *36*(3), 299–328, doi:10.1029/97RG03579.

Gimbert, A. F., V. C. Tsai, T. C. Bartholomaus, M. Jason, and J. I. Walter (2016), Title : Sub-seasonal pressure , geometry and sediment transport changes observed in subglacial channels, *Geophys. Res. Lett.*, *43*(September), 3786–3794, doi:10.1002/2016GL068337.

Gimbert, F., V. C. Tsai, and M. P. Lamb (2014), Journal of Geophysical Research : Earth Surface A physical model for seismic noise generation by turbulent flow in rivers, , 2209–2238, doi:10.1002/2014JF003201.Received.

Haney, M. M. (2014), Backprojection of volcanic tremor, *Geophys. Res. Lett.*, *41*(6), 1923–1928, doi:10.1002/2013GL058836.

Hock, R. (2003), Temperature index melt modelling in mountain areas, *J. Hydrol.*, *282*, 104–115, doi:10.1016/S0022-1694(03)00257-9.

Iken, A., and R. A. Bindschadler (1986), Combined Measurements of Subglacial Water Pressure and Surface Velocity of Findelengletscher, Switzerland: Conclusions About Drainage System and Sliding Mechanism, *J. Glaciol.*, *32*(110), 101–119.

Jones, G. A., B. Kulessa, S. H. Doyle, C. F. Dow, and A. Hubbard (2013), An automated approach to the location of icequakes using seismic waveform amplitudes, *Ann. Glaciol.*, *54*(64), 1–9, doi:10.3189/2013AoG64A074.

Kienholz, C., S. Herreid, J. L. Rich, A. A. Arendt, R. Hock, and E. W. Burgess (2015), Derivation and analysis of a complete modern-date glacier inventory for Alaska and northwest Canada, *J. Glaciol.*, *61*(227), 403–420, doi:10.3189/2015JoG14J230.

Kolmogorov, A. (1941), The local structure of turbulence in incompressible viscous fluid for very large Reynolds numberst, *Akad. Nauk SSSR Dokl*, *30*, 301–305.

Koper, K., and V. Hawley (2010), Frequency Dependent Polarization Analysis of Ambient Seismic Noise Recorded at Broadband Seismometers, *AGU Fall Meet. Abstr.*, *1*, 5.

Koper, K. D., and R. Burlacu (2015), The fine structure of double-frequency microseisms recorded by seismometers in North America, *J. Geophys. Reseach Solid Earth*, 1677–1691, doi:10.1002/2014JB011820.Received.

Larsen, C. F., R. J. Motyka, A. A. Arendt, K. A. Echelmeyer, and P. E. Geissler (2007), Glacier changes in southeast Alaska and northwest British Columbia and contribution to sea level rise, *J. Geophys. Res.*, *112*, doi:10.1029/2006JF000586.

MacAyeal, D. R., Y. Wang, and E. A. Okal (2015), Ambient seismic, hydroacoustic, and flexural gravity wave noise on a tabular iceberg, *J. Geophys. Res. Earth Surf.*, *120*(2), 200–211, doi:10.1002/2014JF003250.

Metaxian, J. P., S. Araujo, M. M. Mora, and P. Lesage (2003), Seismicity related to the glacier of Cotopaxi Volcano, Ecuador, *Geophys. Res. Lett.*, *30*(9), doi:10.1029/2002GL016773.

Mikesell, T. D., K. Van Wijk, M. M. Haney, J. H. Bradford, H. P. Marshall, and J. T. Harper (2012), Monitoring glacier surface seismicity in time and space using Rayleigh waves, , *117*, 1–12, doi:10.1029/2011JF002259.

Motyka, R. J., M. Truffer, E. M. Kuriger, and A. K. Bucki (2006), Rapid erosion of soft sediments by tidewater glacier advance : Taku, *Geophys. Res. Lett.*, *33*, doi:10.1029/2006GL028467.

Nolan, M., R. J. Motyka, K. Echelmeyer, and D. C. Trabant (1995), Ice-thickness measurements of Taku Glacier , Alaska , U.S. A ., and their relevance to its recent behavior, *J. Glaciol.*, *41*(139).

Obara, K. (2002), Nonvolcanic Deep Tremor Associated with Subduction in Southwest Japan, *Science (80-.).*, *296*, doi:10.1126/science.1070378.

Park, J., F. L. I. Vernon, and C. R. Lindberg (1987), Frequency Dependent Polarization Analysis of High-Frequency Seismograms, *J. Geophys. Res.*, *92*, 12,664-12,674.

Pelto, M. S., M. M. Miller, G. W. Adema, M. J. Beedle, S. R. McGee, K. F. Sprenke, and M. Lang (2008), The Equilibrium Flow and Mass Balance of the Taku Glacier , Alaska, 1950-2006, *Cryosph.*, 147–157.

Post, A., and R. J. Motyka (1995), Taku and Le Conte Glaciers, Alaska: Calving-Speed Control of Late-Holocene Asynchronous Advances and Retreats, *Phys. Geogr.*, *16*, 59–82.

Röösli, C., F. Walter, S. Husen, L. C. Andrews, M. P. Lüthi, G. A. Catania, and E. Kissling (2014), Sustained seismic tremors and icequakes detected in the ablation zone of the Greenland ice sheet, *J. Glaciol.*, *60*(221), 563–575, doi:10.3189/2014joG13j210.

Rost, S., and C. Thomas (2002), ARRAY SEISMOLOGY : METHODS AND APPLICATIONS, *Rev. Geophys.*, *40*(3), doi:10.1029/2000RG000100.

Schmandt, B., R. C. Aster, D. Scherler, V. C. Tsai, and K. Karlstrom (2013), Multiple fluvial processes detected by riverside seismic and infrasound monitoring of a controlled flood in the Grand Canyon, *Geophys. Res. Lett.*, *40*(18), 4858–4863, doi:10.1002/grl.50953.

Schmandt, B., D. Gaeuman, R. Stewart, S. M. Hansen, V. C. Tsai, and J. Smith (2017), Seismic array constraints on reach-scale bedload transport, *Geology*, *45*(4), 299–302, doi:10.1130/G38639.1.

Schoof, C. (2010), Ice-sheet acceleration driven by melt supply variability, *Nature*, *468*(7325), 803–806, doi:10.1038/nature09618.

Shreve, R. L. (1972), Movement of Water in Glaciers, *J. Glaciol.*, *11*(62).

Tsai, V. C., B. Minchew, M. P. Lamb, and J.-P. Ampuero (2012), A physical model for seismic noise generation from sediment transport in rivers, *Geophys. Res. Lett.*, *39*(2), 1–6, doi:10.1029/2011GL050255.

Wech, A. G., and K. C. Creager (2008), Automated detection and location of Cascadia tremor, *Geophys. Res. Lett.*, *35*(20), 1–5, doi:10.1029/2008GL035458.

Winberry, J. P., S. Anandakrishnan, and R. B. Alley (2009), Seismic observations of transient subglacial water-flow beneath MacAyeal Ice Stream, West Antarctica, *Geophys. Res. Lett.*, *36*(11), 1–5, doi:10.1029/2009GL037730.

Workman, E., F.-C. Lin, and K. D. Koper (2016), Determination of Rayleigh wave ellipticity across the Earthscope Transportable Array using single-station and array-based processing of ambient seismic noise, *Geophys. J. Int.*, *208*(1), 234–245, doi:10.1093/gji/ggw381.